Nature Communications

https://doi.org/10.1038/s41467-026-73382-9

Article in Press

Giant spin-orbit magnetic state readout enhanced by a magnetic tunnel junction

Received: 20 October 2025

Accepted: 12 May 2026

Cite this article as: Huang, Y., Zhang, K., Liu, G. *et al.* Giant spin-orbit magnetic state readout enhanced by a magnetic tunnel junction. *Nat Commun* (2026). https://doi.org/10.1038/s41467-026-73382-9

Yan Huang, Kun Zhang, Guo Liu, Xiaobai Ning, Shiyang Lu, Shijie Xu, Qing Yang, Wenlong Cai, Renyou Xu, Yuxuan Yao, Yu He, Jinkai Wang, Bo Li, Haozhe Yang, Kewen Shi, Kaihua Cao, Chao Zhao, Yue Zhang & Weisheng Zhao

Giant Spin-Orbit Magnetic State Readout Enhanced by a Magnetic Tunnel Junction

Yan Huang[1,2,3,†], Kun Zhang[1,2,3,†,], Guo Liu[1,2,†], Xiaobai Ning[1,2,†], Shiyang Lu[2,3,†], Shijie Xu[1,2,†], Qing Yang[2,4,†], Wenlong Cai[2], Renyou Xu[2], Yuxuan Yao[2], Yu He[2], Jinkai Wang[1,2], Bo Li[2], Haozhe Yang[2], Kewen Shi[2], Kaihua Cao[2,3], Chao Zhao[2], Yue Zhang[1,2,3,*], and Weisheng Zhao[1,2,3,*]*

[1]State Key Laboratory of Spintronics, Hangzhou International Innovation Institute & School of Integrated Circuit Science and Engineering, Beihang University, Hangzhou 311115, P. R. China.
[2]Fert Beijing Research Institute, MIIT Key Laboratory of Spintronics, School of Integrated Circuit Science and Engineering, Beihang University, Beijing 100191, P. R. China.
[3]Integrated Circuit and Intelligent Instruments Innovation Center, Qingdao Research Institute, Beihang University, Qingdao 266101, P. R. China.
[4]State Key Laboratory of Spintronics Devices and Technologies, School of Integrated Circuits, Nanjing University, Suzhou 215163, P. R. China.
[†]These authors contribute equally to this work.
[*]Correspondence to zhang_kun@buaa.edu.cn; yz@buaa.edu.cn; weisheng.zhao@buaa.edu.cn

Abstract: Magnetoelectric spin-orbit (MESO) logic, composed of a voltage-controlled magnetoelectric writing module and a spin-orbit readout module, is highly expected to substitute the silicon-based transistors and enables energy-efficient and scalable computing. Nevertheless, the output voltage of readout module based on spin-to-charge conversion is far less than the minimum magnetoelectric writing voltage, which greatly restricts the cascading function of MESO logic. Here, we first propose a magnetic tunnel junction (MTJ)-enhanced MESO logic to implement giant readout signal. Up to 1.5 mV output voltage is obtained, marking a significant improvement of approximately two orders of magnitude compared to previous findings. We ascribe the substantial enhancement to current modulation by junction resistance and the spin filtering effect of MgO-based MTJ. Moreover, the naturally integrated MTJ and MESO enables instantaneous and nonvolatile data exchange between computing module and external unit. Our work not only enhances output signal of readout module for direct cascading of MESO logic but also refines the design architecture, marking a pivotal stride forward in propelling MESO technology toward practical applications.

Keywords: Magnetoelectric spin-orbit logic, magnetic tunnel junction, spin-to-charge conversion, spin-orbit coupling, spin polarization

1. Introduction

With technology nodes shrinking, conventional complementary metal-oxide-semiconductor (CMOS) technology faces a growing hurdle in scaling down due to leakage current in the OFF state, imposing a limit on the overall system energy efficiency[1,2]. As a solution, emerging nonvolatile memories, featuring normally-OFF/instantly-ON computation, can overcome the static power brought by leakage current[3–7]. However, because these technologies are not supported to generate an effective driving force, they are hard to drive the subsequent data writing and construct cascaded logic circuits[2,7].

Magnetoelectric spin-orbit (MESO) logic**,** utilizing voltage-controlled magnetoelectric (ME) effect for data writing and spin-orbit coupling (SOC) for magnetic state reading, can be directly cascaded and is regarded as a compelling alternative to CMOS toward 100-mV logic [8,9]. In a MESO logic, a single magnetic layer is used to store bit data, as well as couple writing block (ME block) and reading block (SO block)[8,10]. To date, the quasi-static ferroelectric switching of ME writing module has been achieved down to about 150 mV using ultrathin La-doped $BiFeO_3$, with a pathway to get down to 100 mV[8,11,12]. However, there is a notable challenge that the spin-to-charge conversion (SCC) voltage of readout module is far less than 100 mV, which greatly restricts the cascading function of MESO logic. Typically, this signal measures in the tens or hundreds of milliohms, which results in an output voltage of less than 20 μV[7,13]. The stark discrepancy between the voltages required for writing and those available for reading presents a wide gap to the practical implementation of MESO logics. Although it is predicted using emerging quantum materials such as topological insulators (TIs) and two-dimensional electron gases (2DEGs) could enlarge the SCC signal due to their high SCC efficiency[14–19], experimental results at room temperature (R.T.), to date, have not met the anticipated expectations[20,21]. In addition, the processing compatibility for massive production of these quantum materials has not been totally addressed. Therefore, more brand-new enhancement mechanism of output signal of MESO, different from utilizing high SOC materials, is highly desired to promote the MESO technology towards practical applications.

Here, we propose for the first time the integration of magnetic tunnel junction (MTJ) and MESO by sharing one ferromagnetic (FM) layer as illustrated in Fig. 1a. The proposed device characterizes the same writing process with conventional MESO logic, *i.e.*, V_{in} charges the capacitor of multiferroic material (depicted in dark blue) and when the voltage on ME layer exceeds its threshold, the ferroelectric polarization, interface exchange bias between ME layer and

FM layer, and magnetization of FM layer switch in sequence. MTJ in proposed device acts as an amplifier in reading process, where two different magnetic state of free layer is converted into separated transverse charge signal V_{out}. As shown in Fig. 1b, on the one hand, the injection tunneling current experiences a sudden increase upon the transition of MTJ from antiparallel (AP) to parallel (P) state under a constant voltage supply V_{supply}, *i.e.*, from I_{AP} to I_P. This current alteration can induce an extra voltage signal superposed to the SCC output signal, and amplify the output signal of MESO. On the other hand, the high spin polarization (SP) rate effectuated by the spin filtering mechanism inherent in CoFeB/MgO/CoFeB sandwiched-structure can improve the SCC output voltage. As shown in Fig. 1c, Δ_1 band electrons in sandwiched CoFeB/MgO/CoFeB tunnel easily when the magnetization of two CoFeB layers are parallel alignment, and hard when they are antiparallel, while Δ_2 and Δ_5 band electrons count little[22–25]. Consequently, tunneling current across an MTJ could be highly polarized to significantly enhance SP rate. In addition, we also simplified the MTJ-enhanced MESO logic device into an equivalent circuit to analyze the its operation in the cascaded structure and clarify the writting process in circuit level (Supplementary Note 1). Compared with other MTJ-integrated spin logic devices (*e.g.*, all spin logic and domain-wall-based logic) which utilize spin torques to control input and flowing charges to transmit information, MTJ-enhanced MESO logic is more energy-efficient thanks to ultralow voltage operation[26-28].

Thanks to the current modulation and spin filtering by MTJ, as well as high performance W SOC channel, our experimental findings at R.T. reveal a giant output signal, which is significantly enhanced to an impressive 1.5 mV, about two orders of magnitude greater than that reported in previous literatures[7-10,13,21]. Furthermore, the integrated MTJ can function as a cache memory to provide infinite bandwidth for MESO logic as shown in Fig. 1d, addressing the data exchange issue of computing unit and external memory from the perspective of architecture level, a problem that has been overlooked in previous researches. The proposed “MESO+MTJ” scheme can enhance the output signal and optimize the design architecture, offering a promising direction for future development of MESO technology.

2. Results

2.1 Structural, magnetic and electrical properties

At the outset of our experiments, we examined the impact of the MgO layer thickness on the tunneling magnetoresistance (TMR) ratio, which reveals film quality and SP rate. The functional stacks depicted in Fig. 2a, consisting of W (3.5)/CoFeB (1.9)/MgO (t)/CoFeB (1.9)/CoFe (0.5)/Ru (0.8)/CoFe (2)/IrMn (7.5)/Ru (5), are deposited on bottom electrode Ta (25)/CuN (20) (numbers in parentheses denotes film thickness in nm) with varying MgO thickness *t*. After post annealing at 400 ℃, we determined resistance-area product (RA) and TMR by using current in-plane tunneling (CIPT) measurement at R.T.. The results are shown in Fig. 2b. The RA value increases with increasing MgO thickness, while the TMR ratio exhibits an initial increase followed by a decrease, reaching its maximum when the MgO thickness is 1.1 nm. This optimal TMR value suggests a higher quality of the film and a greater degree of SP[29]. Note that, TMR is expected to appear oscillations as ***t*** keeps increasing due to coherent tunneling and superposition effect of wave functions[30-32].

We then selected a 1.1 nm MgO layer for subsequent experiments, and deposited MTJ stacks directly on thermally oxidized silicon substrate without Ta (25)/CuN (20). Fig. 2c illustrates the hysteresis loop of full functional stacks deposited on thermally-oxidized silicon substrate using vibrating sample magnetometer. By applying an in-plane magnetic field along x direction, distinct magnetic behaviors were observed. The minor loop inset in Fig. 2c indicates that the coercive field of the free layer is approximately 10 Oe.

After a series of electron beam and ultraviolet lithography, as well as etching steps, we have successfully fabricated a junction device featuring multiple electrodes. Fig. 2d illustrates the schematic of proposed MTJ-enhanced MESO readout block. The device features with functional layers of two FM, a SOC, and a tunneling barrier layers. A cross-shape bottom electrode is used to generate transverse output voltage which can be measured between lead 2 and 4, with power supply across lead 0 and 1[7]. Generally, this reading process can be divided into two distinct phases: the spin polarization phase and the SCC phase. During the spin polarization phase, a constant supply source, denoted as V_{supply} or I_{supply}, is applied perpendicularly to the device stacks and injecting a spin polarized current[7]. The injection efficiency is characterized by SP rate. Typically, SP rates are approximately 0.37 for Ni, 0.45 for Co, and 0.43 for Fe, with NiFe and CoFeB exhibiting higher values of 0.48 and 0.53, respectively[33-35]. By applying an external magnetic field and sweeping it along x axis, vertical voltage V_1 (V_{MTJ}) and transverse voltage V_2 (V_{xy}) are both

supposed to appear abrupt changes when free layer magnetization changes, indicating TMR and SCC output signals.

In Fig. 2e, the upper panel shows the top view a junction with an area about 60 nm × 130 nm, while the lower panel gives the side view of junction in which the MgO barrier can be recognized clearly. High-resolution transmission electron microscope image of MTJ stacks also resolves the continuous lattice fringes of MgO barrier, indicating good crystallization (Supplementary Note 2). TMR and SCC signals are shown in Fig. 2f. The low resistance state, corresponding to the alignment of the two magnetic layers at P state, is measured to be around R_{MTJ}^{P} = 4.7 kΩ. Meanwhile, the high resistance state exhibits a resistance of around R_{MTJ}^{AP}= 8 kΩ, corresponding to AP state. Consequently, TMR ratio is calculated to be 70% according to the equation of $TMR = (R_{MTJ}^{AP} - R_{MTJ}^{P})/R_{MTJ}^{P} \times 100\%$. The TMR loss compared with CIPT results can be attributed to damage during nanofabrication. Notably, there are some anomalous points when the external field is around ± 20 Oe, which may be caused by irregular shapes and probable defects and pinnings at the edge of the junction. Meanwhile, we measure transverse voltage V_{xy} versus H_x (V_{xy}-H_x loop) under a constant voltage supply of 300 mV. As expected, there is abrupt changes in transverse signal V_{xy}, precisely at the points where free layer magnetization reverses. Notably, the measurement value of V_{xy} always contains offset signal originating from device structural asymmetry and other undesirable factors. ΔV_{xy}, representing the difference between two magnetic states, is more reasonable to evaluate the output voltage (detailed discussion in Supplementary Note 3). By utilizing MTJ modulation and high SP rate, the observed output voltage ΔV_{xy} at 300 mV supply voltage is approximately 1.5 mV. This result is at least two orders larger than those in previous reports (less than 15 μV in ref[7] and 1.5 μV in ref[13]).

2.2 SCC signal under current source

We performed output signal under a constant current source to precisely evaluate the SCC signal without resistance modulation. The SCC result is intrinsically guaranteed by the anomalous spin-polarized velocity arising from a momentum-space Berry phase of Bloch electrons[36]. Reciprocally, charge-to-spin conversion (CSC), the inverse process of the SCC, can also be assessed using the same device. The charge flowing along W channel would cause spin accumulation and diffusion at and cross interfaces, known as direct spin Hall effect (SHE)[36-39],

which can be detected by magnetic electrodes[7,40]. Through applying current across lead 2 and 4, and measuring voltage between lead 0 and 1, SHE can be evaluated as CSC signal.

In Fig. 3a, we present the SCC curve $\partial V_{24}/\partial I_{01}$ and its inverse, CSC curve $\partial V_{01}/\partial I_{24}$ at 5 μA supply current. The CSC curve appears with opposite polarity to SCC curve, consistent with previous reports[7,40]. This indicates a giant SCC signal $2\Delta R_{SCC}$ around 14.5 Ω, which is nearly 50 times larger than previous reports (0.3 Ω)[7]. However, the CSC signal is about 11 Ω, slightly smaller than SCC signal. We attribute this difference to the spin diffusion and relaxation in z-direction, compared with spin drift in SCC situation[7,40]. The measurement set-up in Fig. 2d also brings various Hall signals mixing in the transverse voltage V_{xy}, such as conventional direct Hall effect, planar Hall effect and anomalous Hall effect[41,42]. Details are discussed in Supplementary Note 4. These Hall signals count less than 0.1 Ω in our nanodot structure, and affect little for the evaluation of final output signal.

The spin polarization phase and the SCC phase are both theoretically bias dependent. At first, the spin injection facilitated by an MTJ could be modulated by its bias-dependent SP[24]. Moreover, considering the ISHE mechanism in SCC phase, the transverse voltage loop of V_2 shall invert polarity when the supply current direction is reversed, that is, $V_2(-I_{supply}, H_x) = -V_2(I_{supply}, H_x)$, resulting no polarity change in resistance versus field curve, that is, $R_{xy}(-I_{supply}, H_x) = R_{xy}(I_{supply}, H_x)$ [43]. As a result, if one obtains $R_{xy}(-I_{supply}, H_x) = -R_{xy}(I_{supply}, H_x)$, this result may be dominated by a current-symmetric term rather than SCC. The second is normally neglected by most researches, but it plays a significant role in SCC signal assessment.

Therefore, we measured different SCC signals by applying currents of varying amplitude and direction, to investigate the bias impact. The SCC signals at ±30 μA appear with the same polarity as expected, but are approximately 2.5 Ω lower than that at 1 μA, as shown in Fig. 3b. Moreover, the signal at +30 μA seems larger than signal at -30 μA. A detailed examination reveals a significant degradation in the SCC signal as supply current is increased, as depicted in Fig. 3c. Interestingly, similar phenomena have been previously reported in W/MgO/CoFeB tri-layer spin-tunneling structure[40]. The maximum SCC signal of $2\Delta R_{SCC}$ is around 14.5 Ω at 5 μA supply. Obviously, when the current amplitudes are equal, the signal obtained under negative bias is slightly smaller than that under positive bias. These observations may imply a bias-dependent SP rate. That is to say, as positive and negative biases activate different energy ranges of electronic

states for tunneling, and regulate the effective barrier height at the two interfaces, amplifying disparities in interface transmission probabilities[44,45].

Consequently, we explored the bias current dependence of the junction resistance R_{MTJ}, and transverse resistance R_{xy}. We use R_{MTJ}^{P} (R_{MTJ}^{AP}) and R_{xy}^{P} (R_{xy}^{AP}) to represent the junction and transverse resistances when MTJ is at P (AP) state, respectively. The findings are summarized in Fig. 3d, where it is noted that while R_{MTJ}^{AP} exhibits a pronounced variation with bias current, R_{MTJ}^{P} remains relatively unchanged. For the transverse resistance R_{xy}, both R_{xy}^{P} and R_{xy}^{AP} exhibit monotonically decreasing trend with the increasing supply current, suggesting an additional mechanism between the SCC and TMR signals. Generally, the SCC signal in our MTJ-enhanced readout module contain two components of information, *i.e.* energetic electrons contribution from reference layer and equilibrium electrons mostly from free layer[40]. The energetic electrons are more energy-sensitive and thus attribute to the bias-dependent signal. These analyses collectively suggest that the utilization of highly spin-polarized electrons tunneling from CoFeB/MgO/CoFeB structures holds greater promise than those from a single FM layer in the development of spin-injection-based devices.

2.3 MTJ-enhanced output signals under voltage source

Then, we compare the output voltage ΔV_{xy} under current source and voltage source. When the applied current source is substituted with a constant voltage V_{supply}, the injection current would experience a sudden decrease upon the transition of MTJ from P to AP state.This alteration consequently affects the output voltage ΔV_{xy}. As illustrated in the inset of Fig. 4a, the maximum observed output voltage ΔV_{xy} is approximately 1.5 mV corresponding to a 300-mV supply voltage, while the largest ΔV_{xy} for current source is about 0.4 mV for 40 μA supply. For a supply voltage of 300 mV, the tunneling current under the P state measures approximately 51 μA. Note that the corresponding current density (6.5×10^{9} A/m^2) is far away from the critical value to induce spin-transfer-torque switching of magnetization in our devices. Given that ΔV_{xy} is proportional to the amplitude of the injection tunneling current, under a supply current of 51 μA, ΔV_{xy} is estimated to be around 0.51 mV, also significantly lower than 1.5 mV. These findings effectively validate the regulation impact of TMR effect when operates under a voltage source.

A comprehensive list of output voltages for various applied currents and voltages is provided in Fig. 4a. It is observed that larger applied source generates larger output voltage, and the voltage

source can yield larger output voltage than current source when the current flow is comparable. Moreover, we could calculate the transverse resistance difference under voltage source. As shown in Fig. 4b, the relationship between ΔR_{xy} and voltage supply exhibits no regularity, quite different from that depicted in Fig. 3c. This is because offset Hall voltage. When this offset is subscribed, ΔR_{xy} trend v.s voltage supply is similar with Fig. 3c, but with larger value (see Supplementary Note 5), meaning an extra term brought by TMR signal, in agreement with our analysis.

To clarify the regulation impact of MTJ, we calculate the relationship between ΔV_{xy} and MTJ parameters under a voltage source as follows,

$$\Delta V_{xy} = \frac{(1+TMR)R_{xy}^{P} - R_{xy}^{AP}}{R_{MTJ}^{AP}} V_{supply} \quad (1)$$

The detailed formula derivation process can be found in Supplementary Note 6. For an MTJ, the parameter I_{AP} is directly determined by the thickness of the MgO barrier. Meanwhile, the TMR ratio critically depends on the overall quality of the MTJ structure. Therefore, to achieve a substantial increase in ΔV_{xy} under a constant voltage source, it is essential to optimize two key factors: 1) the MgO barrier must be sufficiently thin to enhance tunneling efficiency, and reduce R_{MTJ}^{AP}; 2) the crystalline quality of the MTJ must be carefully optimized to ensure large TMR ratio. These demands prefer MgO thickness at first peak of TMR oscillation curve, which also brings maximum conversion efficiency from V_{supply} to V_{out} (see Supplementary Note 7).

Fig. 4c lists some impressive progress in MESO-like readout modules reported so far, containing different SOC materials (heavy metals, TIs and 2DEGs)[7,10,13,20,21,46,47]. Some of them provide output resistance signal ΔR_{xy} with a given current I_{supply}, but no output voltages ΔV_{xy}. As ΔV_{xy} is more critical and essential for practical application, we derive their voltage signals as $\Delta V_{xy} = I_{supply} \times \Delta R_{xy}$ and make a comparison. Although TIs and 2DEGs may remain theoretical superiority thanks to topological surface states and Rashba surface, experimental outputs have no advantages compared with W or Pt based device. One possible reason is their topological state are not stable at R.T. W-based device outputs 3-times larger than Pt-based device as expected, when they are patterned with same size[47]. Interestingly, Pt-based SO device has been reported the most, yet its results vary greatly. The most possible reason is Pt's resistivity in reports varies a lot, from tens of μΩ·cm to hundreds of μΩ·cm[7]. Among all of these proposals, our work not only outperforms all others by a significant margin, but also enhances the output voltage from the microvolt level to the millivolt level, marking a new record. Towards applications, short-term

stability is important for electronic device. In our proposal, the measurement is based on magnetic state readout process, which is quite different from writing stability. The reading stability of our device is similar with that of MTJ, always much better than writing stability[48]. We carried out thousand times of hysteresis loop measurements during 30 days, and results indicate there is no performance degradation (Supplementary Note 8).

2.4 Mechanism Explorations

In this part, we explored possible mechanisms and factors to induce the giant readout signal. As we mentioned in Part 2.1, this reading process is divided into spin polarization phase and SCC phase. For SCC phase, the key factor is performance of W electrode. We performed spin-torque ferromagnetic resonance (ST-FMR) measurement on W/CoFeB (5nm) heterojunction, with different W thickness (Supplementary Note 9). It was found that 3.5 nm W presents as large spin Hall angle as -0.26, promising for high SCC signal.

To investigate spin polarization phase, we compared the output transverse signal in proposed MTJ-enhanced device and traditional FM/SOC-bilayer device. We designed control experiments using 1 μm × 2.5 μm microdot devices with the same channel width of 3 μm. The output signals at I_{supply} = 10 μA of these two samples are shown in Fig. 5a. Sample 1 is a bilayer device composed of W (6)/CoFeB (5), yielding about 2.5 mΩ output signal (Details in Supplementary Note 10). Sample 2 is an MTJ-enhanced device with the above-mentioned film stack structure, which presents approximately 1.2 Ω signal. This difference is quite reasonable according to the numerical model[7]: 1) SP rate of sample 2 is about several times larger than that of sample1; 2) Because there is a phase change when the thickness of W changes from 6 nm to 3.5 nm, the W resistivity in sample 1 is about 60 μΩ·cm and that in sample 2 is about 367 μΩ·cm; 3) The θ_{SH} decreases for W from 0.26 at 3.5 nm to 0.04 at 6 nm[49,50]. These factors give about hundreds times of difference between these two scenarios, as depicted in Fig 5b, quite matching the experiments. More details about the numerical model are presented in Supplementary Note 11.

To further explain the point about SP rates, we established W/CoFe/W and W/CoFe/MgO/CoFe/W atomic-level structure to perform calculation as shown in Fig. 5c and 5d. Detailed structure in the simulation is presented in Methods and Supplementary Note 12. K-resolved transmission spectra in Fig. 5e and 5f illustrate the majority-to-majority tunneling and minority-to-minority tunneling in W/CoFe/W, both generally spreading over the Brillouin zone. In contrast, majority-to-majority tunneling in W/CoFe/MgO/CoFe/W (P state) is concentrated

within a square region around Γ (Fig. 5g), vanishing in the minority-to-minority spectrum (Fig. 5h). Given the definition of spin polarization rate $SP = (G_{\uparrow\uparrow}^{\uparrow} - G_{\uparrow\uparrow}^{\downarrow})/(G_{\uparrow\uparrow}^{\uparrow} + G_{\uparrow\uparrow}^{\downarrow})$, where $G_{\uparrow\uparrow}^{\uparrow}$ is the majority-to-majority spin conductance and $G_{\uparrow\uparrow}^{\downarrow}$ is the minority-to-minority spin conductance[51], the calculated value gives about 92% SP rate for W/CoFe/MgO/CoFe/W structure, about 4 times larger than that for W/CoFe/W. It is evident that several monolayer MgO acts as spin filter to enlarge the difference between majority and minority spin transmission.

In addition, for measurements under voltage source V_{supply}, MTJ not only increases SP, but also modulates injection current between I_{AP} and I_P. The current difference

$$\Delta I = I_P - I_{AP} = V_{supply}\left(\frac{1}{R_{MTJ}^{P}} - \frac{1}{R_{MTJ}^{AP}}\right) = TMR \cdot I_{AP} \quad (2)$$

brings different spin current injection to W channel and induces extra transverse output. This extra term directly enhances ΔV_{xy} and, after subscribing offset voltage, ΔR_{xy} is also enhanced (see Supplementary Note 5).

3. Discussion

Our proposed "MESO+MTJ" scheme effectively overcomes key bottlenecks in MESO logic systems by simultaneously amplifying output signals and redefining data-exchange architectures. This dual advancement manifests in two pivotal aspects:

On the one hand, the output voltage can be further improved to 100 mV to enable the direct cascading of multiple MESO devices. According to equation 1, output voltage conversion efficiency $\Delta V_{xy}/V_{supply}$ is highly related to MTJ properties. With higher TMR, and lower MTJ resistance at AP state, comes higher conversion efficiency. With proper stack design and interface optimization, TMR at R.T. of MTJ can be increased high up to 631%[31]. Meanwhile, high TMR ratio means high spin polarization of injection current. By adapting strong SOC material and scaling down the device size, the SCC process can be further improved. These methods are promising to improve the output voltages to the order of 100 mV.

On the other hand, the "MESO+MTJ" design addresses the critical issue of data exchange between computing unit and peripheral memory from device level (Supplementary Note 13). This device can operate as a logic unit with an intrinsically-integrated high-speed cache memory, as a shared free layer CoFeB is used for logic and memory simultaneously, which resolves the bandwidth mismatch between logic unit and external memory[52]. Moreover, it enables the

extraction of any intermediate process results while simultaneously monitoring its resistance state during computation, which can improve the computation efficiency and reliability.

In addition, CMOS-compatible fabrication of our MTJ-enhanced MESO device is a key point before its practical application. Recently, La-doped $BiFeO_3$ (LBFO) ME films have been successfully grown using magnetron sputtering[53]. Large exchange bias in LBFO/CoFeB heterostructure at room temperature and excellent surface roughness of LBFO have been demonstrated. Thus, in the future studies, the LBFO-based ME writing module and MTJ-enhanced readout module can be integrated together via micro-nano processing technology to construct MTJ-enhanced MESO logic.

In conclusion, our proposal offers a viable pathway toward advancing the real-world implementation of MESO logic technology.

Methods

Film growth and characterization:

All the films used in this work were deposited on 8-inch thermally oxidized silicon substrate, using ultrahigh vacuum *dc/rf* magnetron sputtering system. The substrate was first pre-cleaned for 60 s by Ar^+ ion beam. The CoFe, CoFeB, and IrMn denote $Co_{70}Fe_{30}$, $Co_{60}Fe_{20}B_{20}$, and $Ir_{20}Mn_{80}$ alloy with nominal target compositions, respectively. After deposition, the stacks were in-situ annealed at 400 ℃ for 1 h under an external field of 1 T along x direction to define the reference layer direction and form highly oriented crystalline CoFeB/MgO/CoFeB MTJs. The static in-plane anisotropy magnetization behavior was examined using a vibrating sample magnetometer system.

Device fabrication:

For a nanoscale MTJ-enhanced spin-orbit device, we first patterned 500 nm × 2.5 μm cross-shape channels using standard electron beam lithography (EBL) with maN2403 negative tone photoresist and Ar^+ ion beam etching (IBE). During milling, we monitored the secondary-ion mass spectra. After that, a second round of EBL and IBE procedures were used to define elliptical junctions. Thanks to high-resolution and high-aspect-ratio negative tone photoresist, we successfully formed a photoresist pillar with tens-nanometer length and hundreds-nanometer height. The junction etching was divided into two phases: first, we defined its appearance by small angle (15°) etching until the bottom 3.5-nm-thick W signal appears; second, large angle (75°) etching was utilized to meticulously clean the sidewall re-depositions across the barrier. Rather

than removing the photoresist immediately, we covered the pillars with a 50-nm-thick silicon nitride (Si_3N_4) passivation layer, by using inductively-coupled-plasma chemical vapor deposition, and then followed by lift-off process. Vias through bottom electrodes were formed by standard ultraviolet lithography and inductively coupled plasma reactive ion etching. Ti (10nm)/ Au (100nm) electrodes are finally formed by E-beam evaporation (EBE).

For the microscale SO device, *i.e.*, CoFeB/W readout device and CoFeB/MgO/CoFeB/W MTJ-enhanced readout device, standard ultraviolet lithography and etching process were used to pattern the bottom electrode and the microdot pillar. Then, 50-nm-thick Si_3N_4 passivation layer covered the pillars, and followed by lift-off process. Finally, Ti (10 nm)/Au (100 nm) electrodes are formed by EBE. For bilayer ST-FMR measurement, the device was formed by standard ultraviolet lithography and etching process, with Ti(10 nm)/ Au(100 nm) electrodes using EBE and lift-off process.

Device characterization:

Electronic transport measurements of MTJ-enhanced readout device were conducted on our self-developed probe station, using a Keithley 2182 nanovoltmeter and a Keysight B1500A semiconductor device parameter analyzer under varying in-plane magnetic field. The B1500A is used for direct resistance measurement while 2182 nanovoltmeter is more sensitive and used for transverse voltage measurement. ST-FMR measurement of the bilayer heterojunction was performed using a Keysight MXG N5183B analog signal generator and SR830 lock-in amplifier.

Ab-initio simulation:

The atomic structures are relaxed by Vienna Ab-initio Simulation package (VASP) so that the residual forces are minimized under 0.01 eV/Å[54]. Next, transport calculations are performed by NanoDCAL, which is based on density functional theory (DFT) and Keldysh non-equilibrium Greens function (NEGF)[55]. The physical quantities are represented using a linear combination of atomic orbitals (LCAO) basis with double-zeta plus polarization (DZP) functions. A 20×20×1 k-point mesh is employed in the self-consistent calculation, with the Hamiltonian matrix converged to a tolerance of 10^{-4} eV. Next, the spin-resolved conductance calculation of 500×500×1 was performed to calculate TMR and polarization. The Perdew-Burke-Ernzerhof generalized gradient approximation (PBE-GGA) is selected to describe the exchange-correlation potential, and the cutoff energy of the real space grids is fixed as 3000 eV.

Data availability

The data that support the plots within this paper and the other findings of this study are available from the corresponding author upon reasonable request.

References

1. Tan, C., Tang, J., Gao, X., Xue, C. & Peng, H. 2D bismuth oxyselenide semiconductor for future electronics. *Nat. Rev. Electr. Eng.* **2**, 494–513 (2025).
2. Incorvia, J. A. C. et al. Spintronics for achieving system-level energy-efficient logic. *Nat. Rev. Electr. Eng.* **1**, 700–713 (2024).
3. Chen, M.et al. Ultrawide-bandwidth boron nitride photonic memristors. *Nat. Nanotechnol.* **20**, 1633-1640 (2025).
4. Guo, Z. et al. Spintronics for energy-efficient computing: an overview and outlook. *Proc. IEEE* **109**, 1398–1417 (2021).
5. Khwa, W.-S. et al. A mixed-precision memristor and SRAM compute-in-memory AI processor. *Nature* **639**, 617–623 (2025).
6. Huang, Y. et al. W. Implementation of 16 Boolean logic operations based on one basic cell of spin-transfer-torque magnetic random access memory. *Sci. China. Inf. Sci.* **66**, 1–8 (2023).
7. Pham, V. T. et al. Spin–orbit magnetic state readout in scaled ferromagnetic/heavy metal nanostructures. *Nat. Electron.* **3**, 309–315 (2020).
8. Manipatruni, S. et al. A. Scalable energy-efficient magnetoelectric spin-orbit logic. *Nature* **565**, 35–42 (2019).
9. Vaz, D. C. et al. Voltage-based magnetization switching and reading in magnetoelectric spin-orbit nanodevices. *Nat. Commun.* **15**, 1902 (2024).
10. Lin, C. -C. et al. Experimental demonstration of integrated magneto-electric and spin-orbit building blocks implementing energy-efficient logic. In *2019 IEEE International Electron Devices Meeting (IEDM)*, 37.3.1-37.3.4 (IEEE 2019)
11. Debashis, P. et al. Low-voltage and high-speed switching of a magnetoelectric element for energy efficient compute. In *2022 IEEE International Electron Devices Meeting (IEDM)*, 36.4.1-36.4.4 (IEEE 2022)
12. Luo, B. et al. Magnetoelectric microelectromechanical and nanoelectromechanical systems for the IoT. *Nat Rev Electr Eng* **1**, 317–334 (2024).

13. Vaz, D. C et al. Functional demonstration of a fully integrated magnetoelectric spin-orbit device. In *2021 IEEE International Electron Devices Meeting (IEDM),* 32.4.1-32.4.4 (IEEE 2021)
14. Grezes, C. et al. Non-volatile electric control of spin-orbit torques in an oxide two-dimensional electron gas. *Nat. Commun.* **14**, 2590 (2023).
15. Ding, J. et al. Switching of a magnet by spin-orbit torque from a topological Dirac semimetal. *Adv. Mater.* **33**, 2005909 (2021).
16. Fan, Y. et al. Magnetization switching through giant spin-orbit torque in a magnetically doped topological insulator heterostructure. *Nat. Mater.* **13,** 699–704 (2014).
17. Mellnik, A. R. et al. Spin-transfer torque generated by a topological insulator. *Nature* **511**, 449–451 (2014).
18. Wu, H. et al. Magnetic memory driven by topological insulators. *Nat. Commun.* **12,** 6251 (2021).
19. Vicente-Arche, L. M. et al. Spin-charge interconversion in $KTaO_3$ 2D electron gases. *Adv. Mater.* **33**, 2102102 (2021).
20. Choi, W. Y. et al. All-electrical spin-to-charge conversion in sputtered Bi_xSe_{1-x}. *Nano. Lett.* **22,** 7992–7999 (2022).
21. Gallego, F. et al. All-electrical detection of the spin-charge conversion in nanodevices based on $SrTiO_3$ 2-D electron gases. *Adv. Func. Mater.* **34**, 2307474 (2024).
22. Parkin, S. S. P. et al. Giant tunnelling magnetoresistance at room temperature with MgO (100) tunnel barriers. *Nat. Mater.* **3**, 862–867 (2004).
23. Yuasa, S. & Djayaprawira, D. D. Giant tunnel magnetoresistance in magnetic tunnel junctions with a crystalline MgO(001) barrier. *J. Phys. D: Appl. Phys.* **40**, R337-R354 (2007).
24. Yuasa, S., Nagahama, T., Fukushima, A., Suzuki, Y. & Ando, K. Giant room-temperature magnetoresistance in single-crystal Fe/MgO/Fe magnetic tunnel junctions. *Nat. Mater.* **3**, 868–871 (2004).
25. Mathon, J. & Umerski, A. Theory of tunneling magnetoresistance of an epitaxial Fe/MgO/Fe(001) junction. *Phys. Rev. B* **63**, 220403 (2001).
26. Behin-Aein, B., Datta, D., Salahuddin, S. & Datta, S. A. Proposal for an all-spin logic device with built-in memory. *Nat. Nanotechnol.* **5**, 266-270 (2010).

27. Raymenants, E. et al. Nanoscale domain wall devices with magnetic tunnel junction read and write. *Nat. Electron.* **4**, 392-398 (2021).
28. Baek, S. H. C. et al. Complementary logic operation based on electric-field controlled spin–orbit torques. *Nat. Electron.* **1**, 398-403 (2018).
29. Julliere, M. Tunneling between ferromagnetic films. *Phys. Lett. A* **54**, 225–226 (1975).
30. Wang, W. et al. Coherent tunneling and giant tunneling magnetoresistance in Co_2FeAl/MgO/CoFe magnetic tunneling junctions. *Phys. Rev. B* **81**, 140402 (2010).
31. Scheike, T., Wen, Z., Sukegawa, H. & Mitani, S. 631% room temperature tunnel magnetoresistance with large oscillation effect in CoFe/MgO/CoFe(001) junctions. *Appl. Phys. Lett.* **122**, 112404 (2023).
32. Masuda, K., Scheike, T., Sukegawa, H., Kozuka, Y., Mitani, S. & Miura, Y. Theory for tunnel magnetoresistance oscillation. *Phys. Rev. B* **111**, L220406 (2025).
33. Strijkers, G. J., Ji, Y., Yang, F. Y., Chien, C. L. & Byers, J. M. Andreev reflections at metal/superconductor point contacts: measurement and analysis. *Phys. Rev. B* **63**, 104510 (2001).
34. Kaiser, C. & Parkin, S. S. P. Spin polarization in ferromagnet/insulator/superconductor structures with the superconductor on top of the barrier. *Appl. Phys. Lett.* **84**, 3582–3584 (2004).
35. Paluskar, P. V. et al. Spin tunneling in junctions with disordered ferromagnets. *Phys. Rev. Lett.* **100**, 57205 (2008).
36. Sinova, J., Valenzuela, S. O., Wunderlich, J., Back, C. H. & Jungwirth, T. Spin Hall effects. *Rev. Mod. Phys.* **87**, 1213–1260 (2015).
37. Peng, S. et al. Unconventional scaling of the orbital Hall effect. *Nat. Mater.* 1–7 (2025).
38. Zheng, Z. et al. All-electrical perpendicular switching of chiral antiferromagnetic order. *Nat. Mater.* **24**, 1407-1413 (2025).
39. Takeuchi, Y. et al. Electrical coherent driving of chiral antiferromagnet. *Science* **389**, 830–834 (2025).
40. Liu, L., Chen, C.-T. & Sun, J. Z. Spin Hall effect tunnelling spectroscopy. *Nat. Phys.* **10**, 561–566 (2014).

41. Groen, I., Pham, V. T., Leo, N., Marty, A., Hueso, L. E. & Casanova, F. Disentangling spin, anomalous, and planar Hall effects in ferromagnet–heavy-metal nanostructures. *Phys. Rev. Appl.* **15**, 044010 (2021).
42. Mizuno, H., Isshiki, H., Kondou, K., Zhu, Y. & Otani, Y. Influence of planar Hall effect on the output signal in a T-shaped spin conversion device. *Appl. Phys. Let.* **119**, 0061147 (2021).
43. Pashenkin, I. Y., Sapozhnikov, M. V., Gusev, N. S., Karashtin, E. A. & Fraerman, A. A. Extrinsic tunnel Hall effect in MgO-based tunnel junctions. *Phys. Rev. B* **106**, L220408 (2022).
44. Xiang, X. H., Zhu, T., Du, J., Landry, G. & Xiao, J. Q. Effects of density of states on bias dependence in magnetic tunnel junctions. *Phys. Rev. B* **66**, 174407 (2002).
45. Kalitsov, A. et al. Bias dependence of tunneling magnetoresistance in magnetic tunnel junctions with asymmetric barriers. *J. Phys.: Condens. Matter.* **25**, 496005 (2013).
46. Teresi, S. et al. Spin-orbit readout using thin films of topological insulator Sb_2Te_3 deposited by industrial magnetron sputtering. *Adv. Func. Mater.* **33**, 02303878 (2023).
47. Lin, Y.-L. et al. Scalable spin-to-charge conversion device with nanopatterning. *ACS Appl. Electron. Mater.* **6**, 6657–6664 (2024).
48. Kuroiwa, T., Takenaga, T., Sadeh, B., Kobayashi, H., & Sato, K. Read-cycle endurance of magnetic random access memory elements. *IEEE Trans. Magn.* **40**, 2631-2633 (2004).
49. Pai, C.-F., Liu, L., Li, Y., Tseng, H. W., Ralph, D. C. & Buhrman, R. A. Spin transfer torque devices utilizing the giant spin Hall effect of tungsten. *Appl. Phys. Lett.* **101**, 122404 (2012).
50. Sriram, K., Mondal, R., Pradhan, J., Haldar, A. & Murapaka, C. Structural phase engineering of (α+β)-W for a large spin Hall angle and spin diffusion length. *J. Phys. Chem. C* **127**, 22704–22712 (2023).
51. Sun, H.-H. et al. Majorana zero mode detected with spin selective Andreev reflection in the vortex of a topological superconductor. *Phys. Rev. Lett.* **116**, 257003 (2016).
52. McKee, S. A. Reflections on the memory wall. In *2004 Computer Frontiers Conference*, p. 162 (ACM Press, 2004).
53. Zhou, Z. et al. Magnetron sputtering synthesis of La-Doped $BiFeO_3$ thin films and enhanced exchange bias in CoFeB/$Bi_{1-x}La_xFeO_3$ heterostructures, *Adv. Phys. Res.* e00113 (2025).
54. Hafner, J. Ab-initio simulations of materials using VASP: Density-functional theory and beyond. *J. Comput. Chem.* **29**, 2044–2078 (2008).

55. Taylor, J., Guo, H. & Wang, J. Ab initio modeling of quantum transport properties of molecular electronic devices. *Phys. Rev. B* **63**, 245407 (2001).

Acknowledgements

We thank Y. Han (Center of Nanofabrication, Tsinghua University) for micro-nano fabrication technical assistance.

Funding

This work was supported by the National Natural Science Foundation of China (92164206, 52261145694, and 62401026), National Key Research and Development Program of China (2024YFE0203400) and Beijing Natural Science Foundation (L234081).

Author contributions

W.S.Zhao, Y.Zhang, and K.Zhang supervised the project; Y.Huang, K.Zhang, G.Liu and X.B.Ning conceived the idea; S.Y.Lu, Y.X.Yao, Y.He and B.Li deposited the films, Y.Huang, G.Liu, and S.J.Xu fabricated the devices with help from K.W.Shi, K.H.Cao and C.Zhao; S.Y.Lu implemented the VSM measurement; Y.Huang, G.Liu, K.Zhang, W.L.Cai and R.Y.Xu implemented the DC measurement setup; Y.Huang, G.Liu and Q.Yang implemented the DC measurement and analyzed the data with help from S.J.Xu, K.Zhang, Y.Zhang, W.S.Zhao and H.Z.Yang; X.B.Ning carried out ab-initio simulations; Q.Yang carried out finite element simulations; J.K.Wang provided circuit-level suggestions. All the authors read and commented on the manuscript.

Competing interests

The authors declare no conflict of interest.

Fig. 1| Concept of MTJ-enhanced MESO logic. a) Structure schematic of MTJ-enhanced MESO. The device formed with a magnetoelectric (ME) layer, two ferromagnetic (FM) layers, a spin injection (SI) layer, a spin-orbit-coupling (SOC) layer, a tunnel barrier and metal connect (MC). b) Principles of tunneling current modulation by MTJ resistance. The tunneling current shrinks when MTJ changes form P state to AP state. c) Principles of spin filtering effect, where Δ_1 band electron with nearly 100% spin polarization is allowed to be injected. d) Data-exchange architecture of "MTJ+MESO" schemes.

Fig. 2| Structure optimization and basic device properties. a) Schematic of multilayer film stacks. All numbers are in nm with varied MgO thickness t. b) RA and extracted film TMR ratio as a function of MgO thickness t. c) In-plane hysteresis loop of stacks in (a) with 1.1 nm MgO. Inset: minor loop of free layer behavior. d) Schematic of MTJ-enhanced reading module and device measurement set-up, where TMR and SCC signal are simultaneously obtained. e) Top view (upper panel) of a 60 nm×130 nm junction and side view (lower panel). The well-crystallized MgO can be easily recognized. f) Junction resistance under 1 μA supply current and transverse voltage under 300 mV supply voltage versus x axis magnetic field along.

Fig. 3| Output signal characterization under current source. a) SCC signal $\partial V_{24}/\partial I_{01}$ and its reciprocal CSC signal $\partial V_{01}/\partial I_{24}$ as a function of external field with 5 μA supply current. b) Normalized transverse resistance versus external field under different supply current. c) $2\Delta R_{SCC}$ as a function of supply current. d) MTJ resistance and transverse output resistance at different state as a function of supply current.

Fig. 4| Output signals under different sources. a) Output voltage comparison between voltage supply and current supply. Inset: Transverse voltage under 300 mV v.s. that under 40 μA. b) Resistance outputs at different supply voltages. c) Benchmark of output signals of MESO-like device for different materials and configurations until now.

Fig. 5| Control samples and mechanism analysis. a) Output resistance signal comparisons between W/MTJ device and W/CoFeB-bilayer device using microdot device. b) Numerical simulations for the bilayer and multilayer structure using physical parameters in experiments. c) and d) Layer structures of W/CoFe/W and W/CoFe/MgO/CoFe/W for ab-initio calculations. e) and f) Majority-to-majority and minority-to-minority transport for W/CoFe/W. g) and h) Majority-to-majority and minority-to-minority transport for W/CoFe/MgO/CoFe/W.

Editor's Summary
This work proposes an MTJ-enhanced magnetoelectric spin-orbit (MESO) logic architecture for giant spin-orbit magnetic state readout. The device achieves a room-temperature output voltage up to 1.5 mV and instant and efficient data exchange between computing and memory units.

Peer review information: *Nature Communications* thanks Sicong Zhu and the other anonymous reviewer(s) for their contribution to the peer review of this work. A peer review file is available.

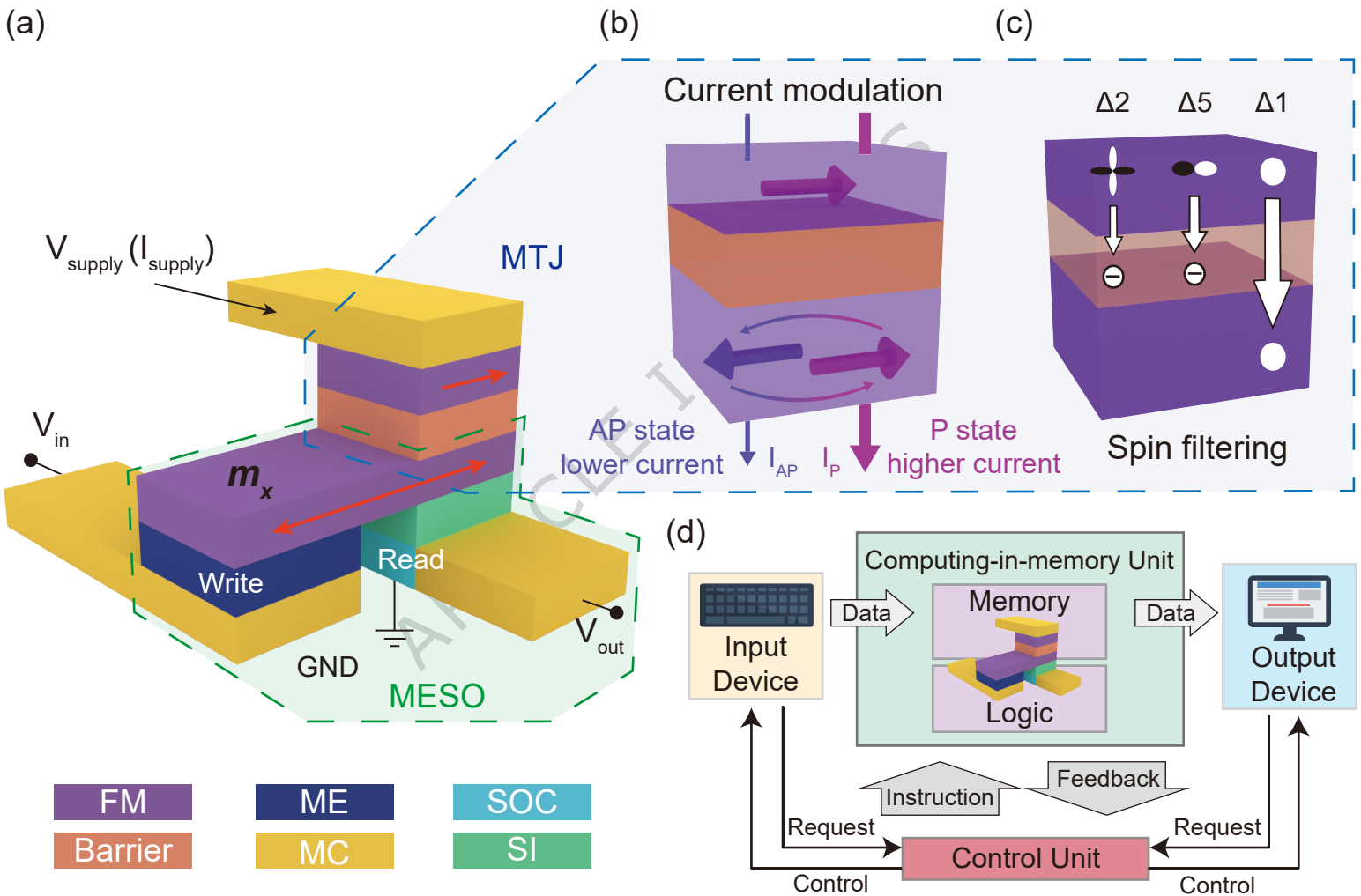
(a)
(b)
(c)
(d)
MTJ
V_{supply} (I_{supply})
V_{in}
m_x
Write
Read
GND
V_{out}
MESO
Current modulation
AP state
lower current
I_{AP}
I_P
P state
higher current
Δ2
Δ5
Δ1
Spin filtering
FM
Barrier
ME
MC
SOC
SI
Computing-in-memory Unit
Memory
Logic
Input Device
Data
Data
Output Device
Instruction
Feedback
Request
Request
Control Unit
Control
Control

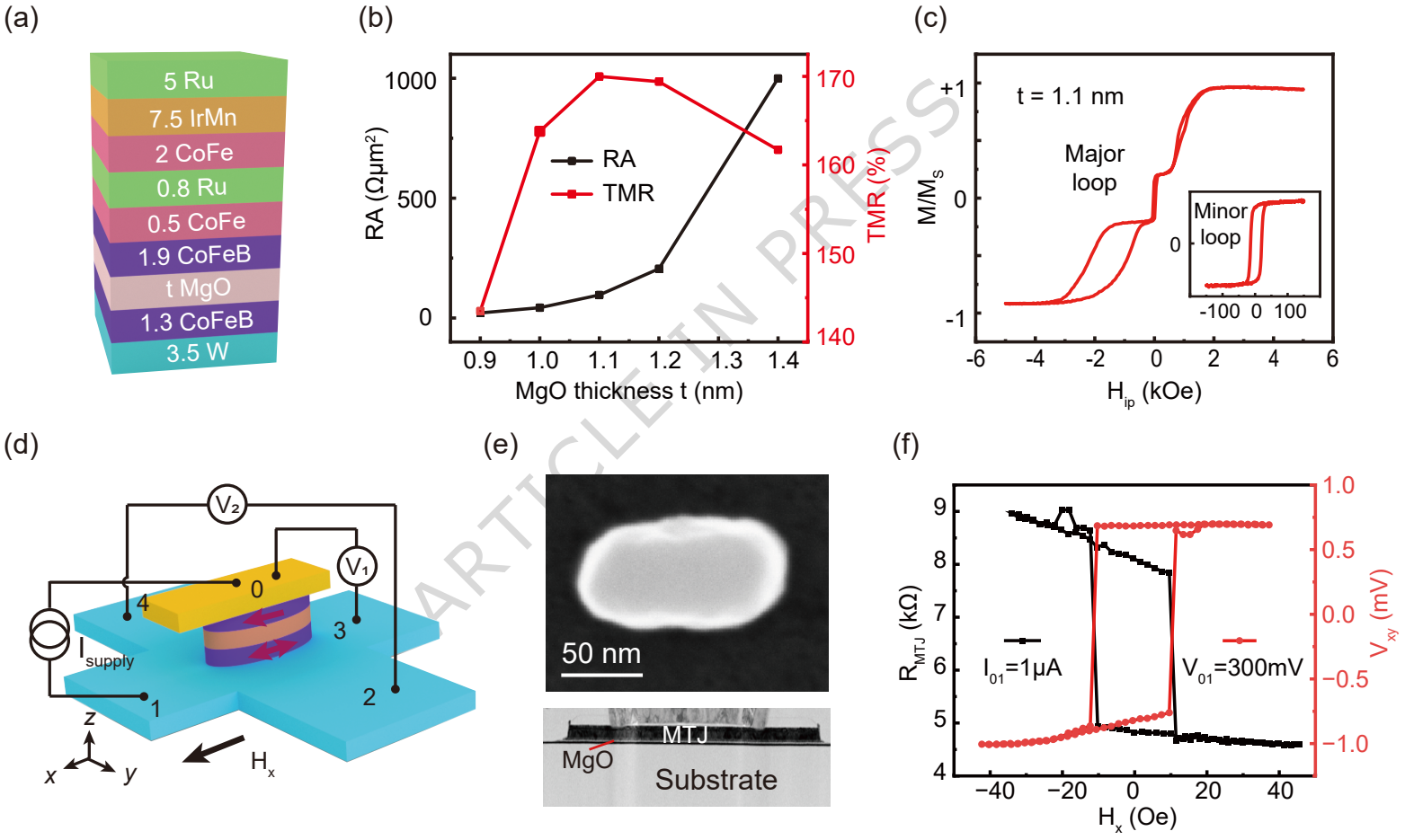

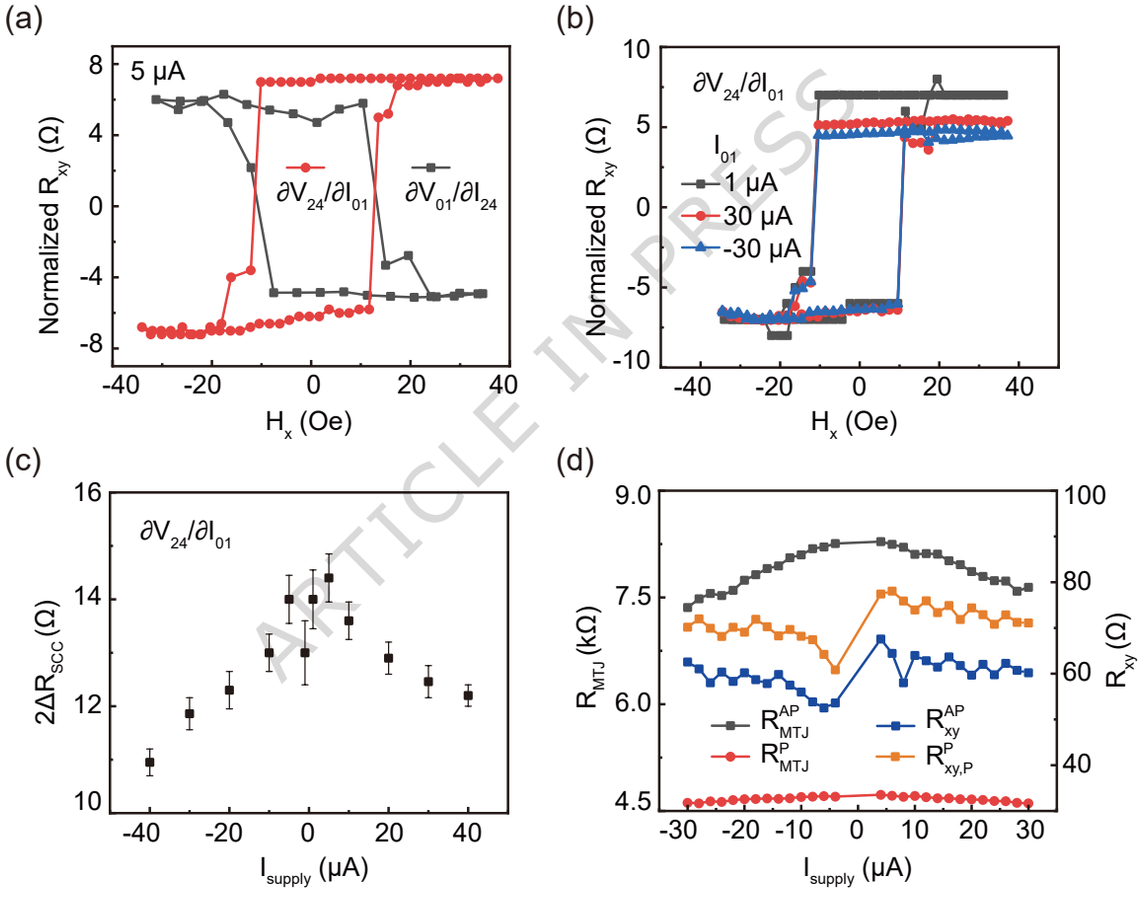

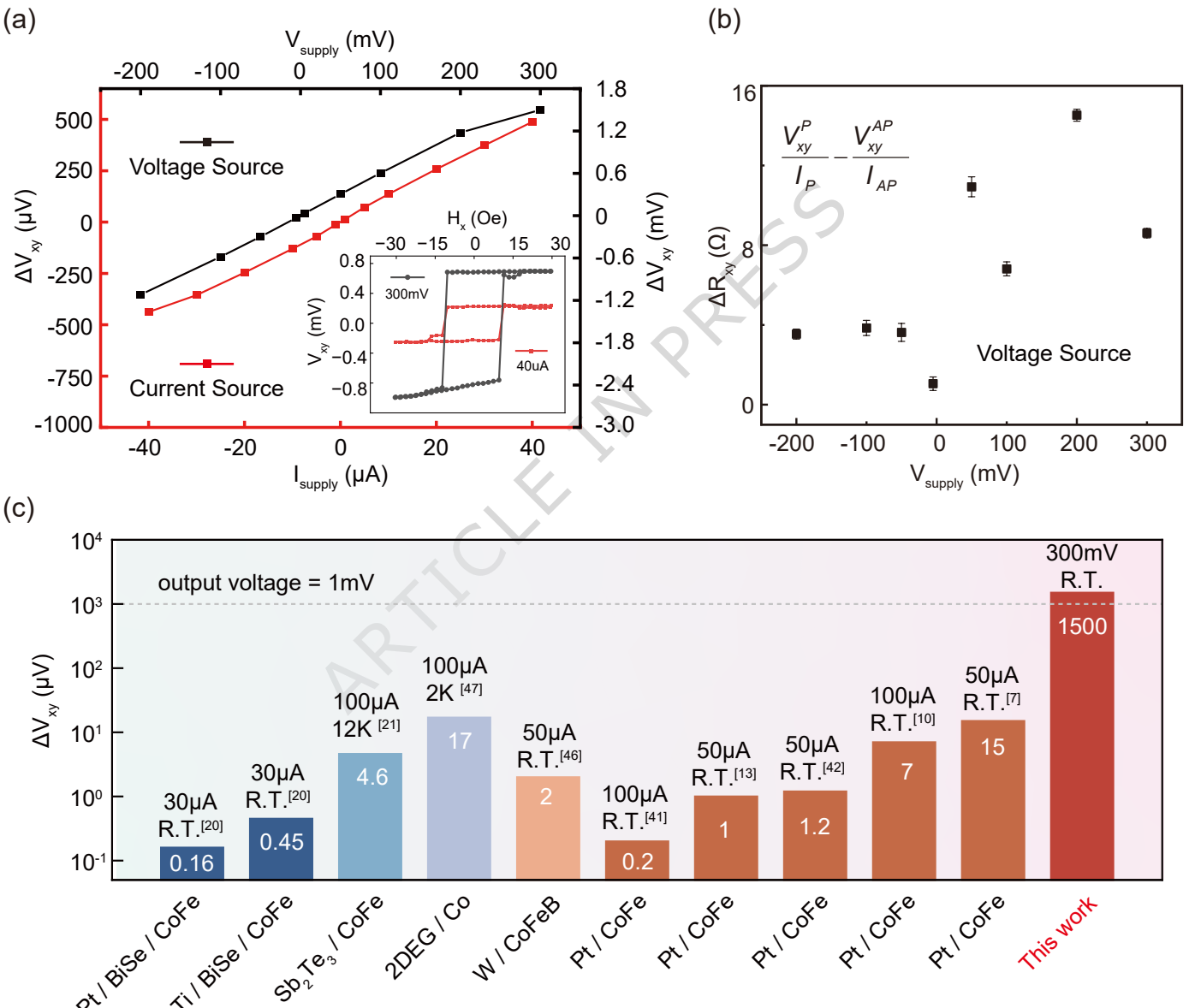

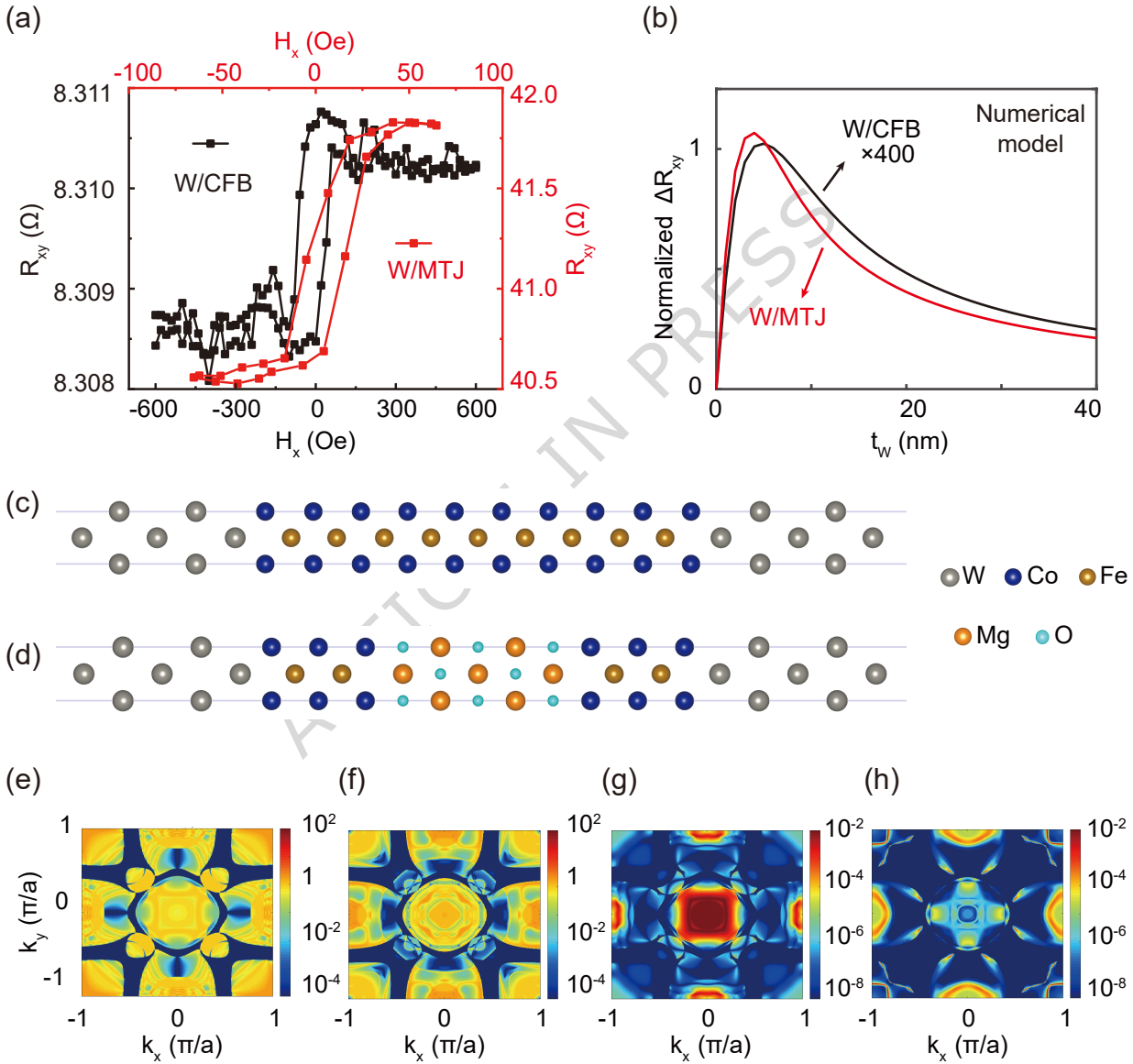
(a)
H_x (Oe)
-100
-50
0
50
100
8.311
8.310
8.309
8.308
R_xy (Ω)
42.0
41.5
41.0
40.5
R_xy (Ω)
W/CFB
W/MTJ
-600
-300
0
300
600
H_x (Oe)
(b)
Numerical model
W/CFB ×400
W/MTJ
Normalized ΔR_xy
1
0
0
20
40
t_W (nm)
(c)
(d)
W
Co
Fe
Mg
O
(e)
(f)
(g)
(h)
k_y (π/a)
1
0
-1
10^2
1
10^-2
10^-4
10^-6
10^-8
-1
0
1
k_x (π/a)